Microstructural evolution of uranium dioxide following compression creep tests: An EBSD and image analysis study

X. Iltis, Nathalie Gey, C. Cagna, Alain Hazotte, Philippe Sornay

Microstructural evolution of uranium dioxide following compression creep tests: An EBSD and image analysis study

X. Iltis [a,*], N. Gey [b], C. Cagna [a], A. Hazotte [b], Ph. Sornay [a]

[a] CEA, DEN, DEC, Cadarache, 13108 Saint-Paul-Lez-Durance, France
[b] Laboratoire d'Etude des Microstructures et de Mécanique des Matériaux (LEM3), CNRS UMR 7239, Université de Lorraine, Ile du Saulcy, 57045 Metz Cedex 1, France

HIGHLIGHTS

- Image analysis and EBSD are performed on creep tested UO_2 pellets.
- Development of intergranular voids, with increasing strain, is quantified.
- EBSD evidences a sub-structuration process within the grains and quantifies it.
- Creep mechanisms are discussed on the basis of these results.

ABSTRACT

Sintered UO_2 pellets with relatively large grains (~25 μm) are tested at 1500 °C under a compressive stress of 50 MPa, at different deformation levels up to 12%. Electron Back Scattered Diffraction (EBSD) is used to follow the evolution, with deformation, of grains (size, shape, orientation) and sub-grains. Image analyses of SEM images are performed to characterize emergence of a population of micron size voids. For the considered microstructure and test conditions, the results show that the deformation process of UO_2 globally corresponds to grain boundary sliding, partly accommodated by a dislocational creep within the grains, leading to a highly sub-structured state.

1. Introduction

In nuclear power plants, uranium dioxide fuel pellets undergo viscoplastic deformation by creep mechanisms, especially during power transients [1]. These deformation phenomena are involved in the Pellet–Cladding Interaction (PCI) processes, which can under certain circumstances induce failure of the zirconium alloy cladding [2].

In order to get a better understanding of the mechanical behaviour of UO_2 fuel, numerous out of pile tests have been performed in the past. Most of them, for certain conducted more than 30 years ago, correspond to compressive tests in a temperature range between 1000 °C and 2000 °C (1000 °C corresponding roughly to the brittle to ductile transition for UO_2 [3]) and a stress range between 5 and 150 MPa [4–7]. The creep rate is then analysed at constant temperature as a function of stress which enables power laws to be established. Two regimes are usually identified: a first one, at "low" stresses corresponding to a stress exponent of about 1 and a second one, at "high" stresses, corresponding to an exponent of about 4 or 5 (experimental data being in fact highly scattered since stoichiometry and/or impurities strongly affect the creep behaviour of UO_2). There remains some uncertainty as to mechanisms involved in these two regimes. In most of studies, the first regime is described as involving diffusional deformation mechanisms (so called "diffusional creep"), whereas in the second one, dislocation motion is considered ("dislocational creep").

In fact, relatively few studies make a link between these power laws and the evolution of the UO_2 microstructure with deformation. One of the more complete and recent ones is that performed by Dherbey et al. [6]. In this work, Scanning Electron microscopy (SEM) micrographs enabled the development of intergranular voids to be qualitatively followed as a function of deformation. However, these voids where not quantitatively characterized in terms of size, number and orientation (with respect to the loading direction). Transmission electron microscopy (TEM) was also used to study dislocation behaviour: the development of sub-boundaries was evidenced, but this phenomenon was not linked to local characteristics such as grains orientations and was not quantified either.

Our work is aimed at providing a more detailed description of the damage process in sintered UO_2 during creep tests in the "high

* Corresponding author. Tel.: +33 442256497.
E-mail address: xaviere.iltis@cea.fr (X. Iltis).

Table 1
Deformation levels and test durations of the samples.

Sample identification number	Mean global deformation (%)	Duration of the stress holding, at 1500 °C (h)
1	0	0
2	2.6	0.1
3	8.0	2.7
4	12.0	6.6

stress" region, corresponding to that in which dislocations are involved in the deformation process. For this purpose, UO_2 pellets with relatively large grains (~25 μm) are tested at 1500 °C under a compressive stress of 50 MPa at three different deformation levels up to 12%. Image analyses of SEM micrographs are performed to characterize the emergence of a micron size void population. Electron Back Scattered Diffraction (EBSD) is used to follow the evolution of grains (size, shape, orientation) and sub-grains as a function of creep strain. This method is now largely used for studying metallic alloys and technical ceramics (see for example [8,9]) but its application on UO_2 is relatively new: only a few papers are available (see, for example: [10–13]), none of them, to the best of our knowledge, deals with mechanically tested samples. Its potential in this research field will therefore also be discussed in this work.

2. Experimental details

2.1. UO_2 pellet manufacturing and characteristics

The pellets used in this study were taken from a previous work in which an extensive description of their manufacturing conditions and characteristics was provided [14].

An UO_2 powder, obtained by a standard dry route process was used. This powder was disagglomerated by crushing, in order to obtain particles with a mean diameter of 0.7 μm, measured by laser granulometry. The powder was then pressed uniaxially under 400 MPa to obtain green pellets. A sintering heat treatment was performed at 1900 °C for 4 h, under an atmosphere of Ar + 5%H_2 to obtain stoichiometric pellets (diameter: 8 mm, height: 12 mm) with a mean density of 0.986 (standard deviation: 0.02) of the theoretical UO_2 density, measured by an immersion method. The mean grain size, measured by image analysis on SEM micrographs is of the order of 25 μm.

2.2. Compression creep tests

Creep tests were performed under uniaxial compression in a furnace adapted on a screw-type Instron® machine, at a temperature of 1500 °C, under 50 MPa and for strains ranging from 0% to 12% (Table 1). According to a previous work, the critical load for which the "high stress" creep stage is effective at 1500 °C is of the order of 30 MPa for this material [14]. Therefore, tests were conducted in the so called dislocational or high stress creep regime. The atmosphere was the same as that used during the sintering heat treatment, to maintain a material close to stoichiometry.

During the test, the pellets underwent a heterogeneous barrel type deformation. This is a structural effect, since the extremities of the sample are blocked between two compression plates, leading to a non-uniform deformation of the pellet [3]. The vertical displacement was measured differentially using two extensometers, one at the top and the other at the bottom of the pellet. The deformation values gathered in Table 1 are therefore necessarily average values. In this table, sample 1 corresponds to the "as sintered" state and is our reference state.

2.3. Sample preparation and characterization

Samples were cut longitudinally (i.e. parallel to the compression direction) with a diamond wire saw to obtain a piece of about 8 × 12 × 1 mm, taken from the central part of the pellet. This piece was mechanically polished. The final polishing step was performed with a 0.04 μm silica aqueous suspension (OP-U, Struers) to minimize the polishing superficial damage for EBSD characterizations and to improve the orientation contrast on Back Scattered Electron (BSE) images.

SEM micrographs (pixel size: 0.15 μm), in BSE (back-scattered electron) mode, were taken with a FEI XL 30 FEG microscope, in the central part of each sample, i.e. in the most deformed area. Additional high resolution BSE images were acquired with a ZEISS Supra 40 SEM to reveal dislocation arrangements at low angle boundaries [15]. Four areas of about 0.61 × 0.45 mm were analysed per sample, leading to a total examined zone of about 1 mm^2. On these micrographs, dark details (holes) corresponding both to fabrication pores (small and rounded) and to intergranular voids induced by the creep process (larger and elongated) were examined: cf. Fig. 1. We used the AnalySIS image analysis software to impose a threshold on the grey level image which we subsequently binarised. This enabled us to extract dark details characteristics from the image such as:

- size: defined by the detail area or its Equivalent Circular Diameter (ECD),
- shape: defined by the detail aspect ratio (ratio of major over minor axis of fitted ellipse),
- morphological orientation with respect to the compression axis: defined by the angle between the compression axis and the direction of maximum projected diameter (also called Feret diameter), a zero angle value corresponding to a direction parallel to the compression one.
- These measurements, carried out first on the reference sample, showed that fabrication pores are characterized by:

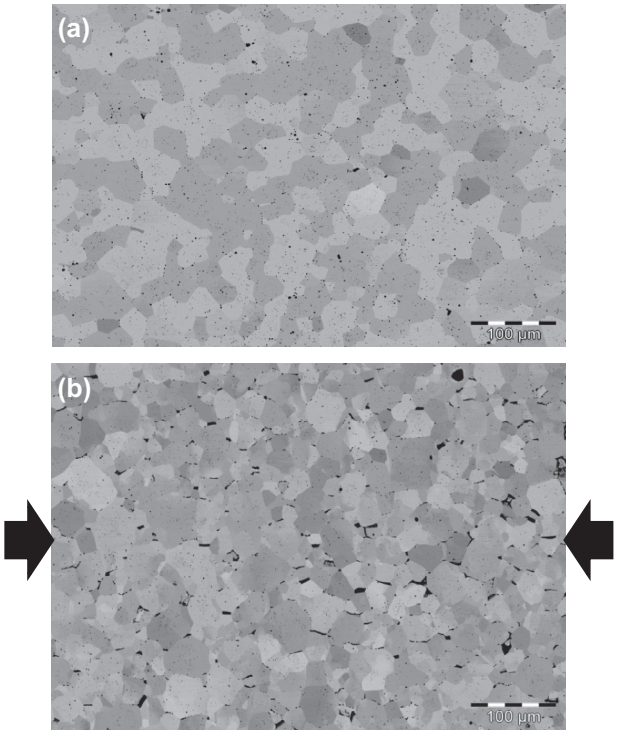

Fig. 1. SEM micrographs, in BSE mode of (a) sample 1 (reference) and (b) sample 3 (deformed at 8%). Black arrow in (b) indicate the compression direction.

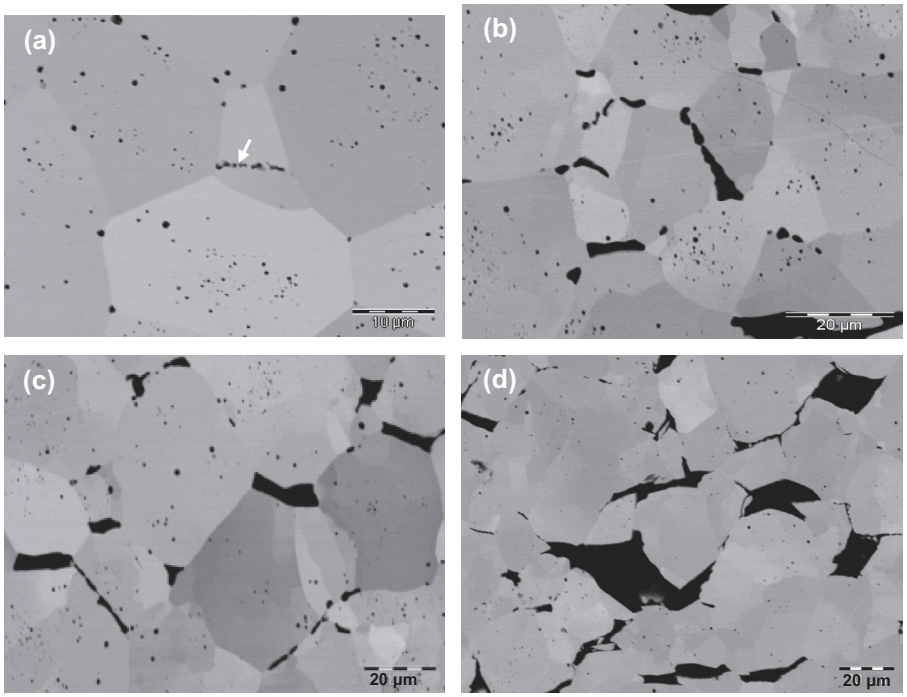

Fig. 2. Observation of creep voids in (a) sample 2 (deformed at 2.6%), (b) and (c) sample 3 (deformed at 8%) and (d) sample 4 (deformed at 12%) – SEM micrographs in BSE mode.

– an area below 10 µm^2 (that is: an ECD below 1.8 µm),
– an aspect ratio below 2, for 90% of them.

These characteristics were used to discriminate fabrication pores (which were subtracted from the dark details revealed following the binarisation of the image) and voids resulting from the damage processes the mechanically tested samples are subjected to, assuming that the as-fabricated pores do not significantly change in size during the creep test. These criteria are obviously not ideal, especially when considering small voids obtained at low deformation levels (case of sample 2) but have enabled us none the less to analyse our experimental results and draw general conclusions.

EBSD maps were performed with the FEI XL 30 FEG SEM (accelerating voltage: 20 kV, beam current: 1 nA) by means of a Nordlys II Nano camera from Oxford Instruments driven by the AZTEC software. EBSD data were analysed with the Channel 5 suite of programs [16]. The indexation rate of EBSD data (ratio of indexed pixels over total number of tested pixels) varied from 92% to 98.5% (prior to any data cleaning, with a mean angular deviation lower than 0.5°, between the detected Kikuchi bands and the simulation), depending on the acquisition step and the number and size of pores and voids present in the examined area. Two main types of maps were acquired:

– global maps at relatively low magnification (×150), to get information concerning the grain characteristics (size of the map: about 2.02 × 1.45 mm^2, acquisition step: 2 µm),
– local maps at higher magnification (×500), to study local effects in relation to void formation sites at grain boundaries, and the substructures within the grains (size of the map: about 0.61 × 0.45 mm^2, acquisition step: 0.3 µm).

The angular resolution of EBSD maps was between 0.5° and 1°, depending on the quality of the sample preparation and the EBSD acquisition conditions. A careful noise reduction procedure was applied to all EBSD maps, with a limited extrapolation level of zero solution points, in order to avoid filling intergranular voids (that of some small fabrication pores being unavoidable).

Grain sizes were determined according to a standard [17]. At least 5000 grains per sample were measured. The critical disorientation angle chosen to define a grain boundary was 5°. The accuracy of the grain size measurements is estimated at ±10%, in accordance with the estimation given in the standard and the laboratory feedback.

The compression axis is horizontal in all images (SEM micrographs, EBSD maps) presented in the next section.

3. Results

3.1. Damage evolution of UO_2 under compression creep

Grain boundary damage begins with the nucleation and growth of round shaped voids and evolves to form large cracks as strains increase.

Fig. 2 shows SEM micrographs revealing typical void morphologies found in the three mechanically tested samples. At the lowest deformation level, an accumulation of small rounded voids which are close to connecting up is observed along only a few grain boundaries (cf. Fig. 2a: white arrow). At 8% deformation level, voids are now much larger and more numerous. Two morphologies are encountered: percolating rounded voids and larger angular ones, probably corresponding to the decohesion of contiguous grains (Fig. 2b and c). Finally, at a deformation level of 12%, only large angular voids which propagate over different triple points are observed (Fig. 2d). This gradual evolution of the intergranular void morphology, with increasing strain, points to at least two different deformation processes.

The void size evolution with strain is summarised in Fig. 3. The number of small voids (ECD class: 0–3 µm) increases sharply up to 8% deformation, occupying only a small surface fraction. At higher

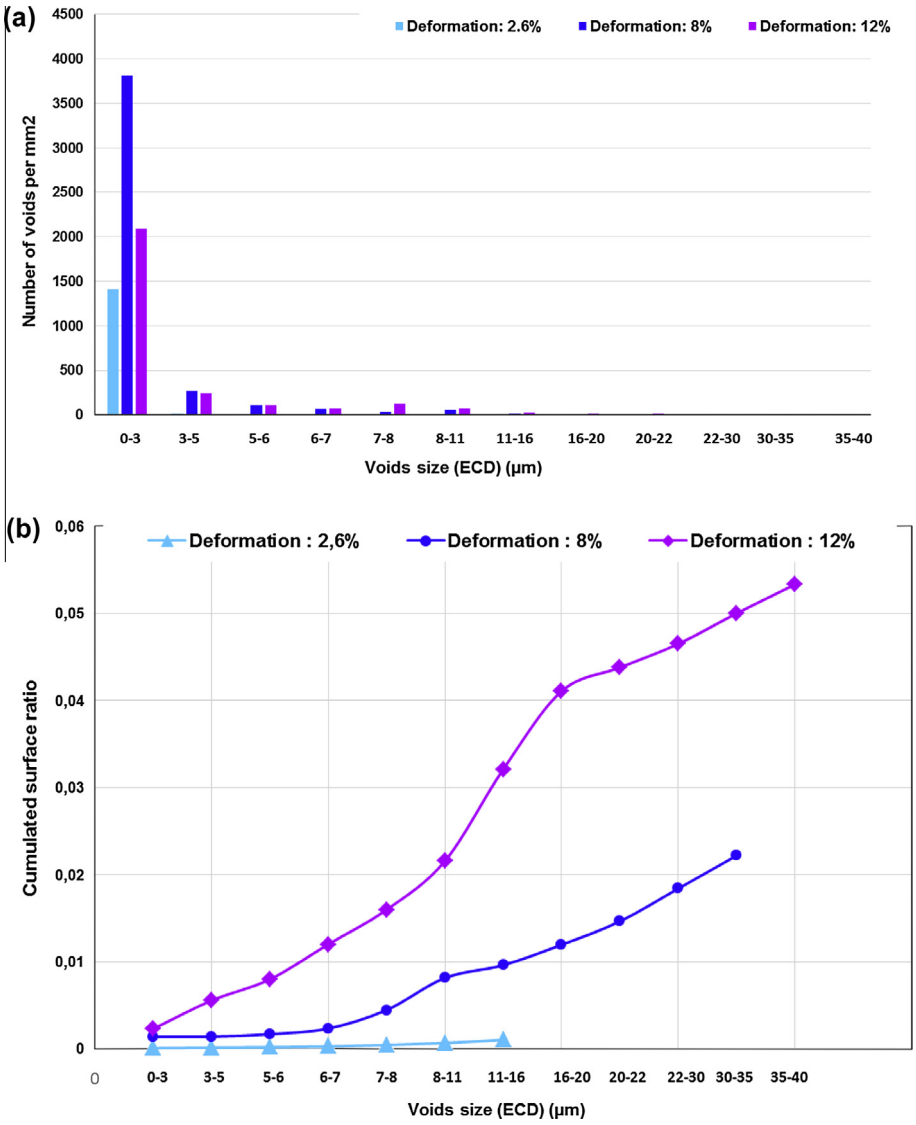

Fig. 3. Characterization of creep voids by image analysis, in the three mechanically tested samples: results represented (a) in number per mm^2 and (b) in cumulated surface ratio.

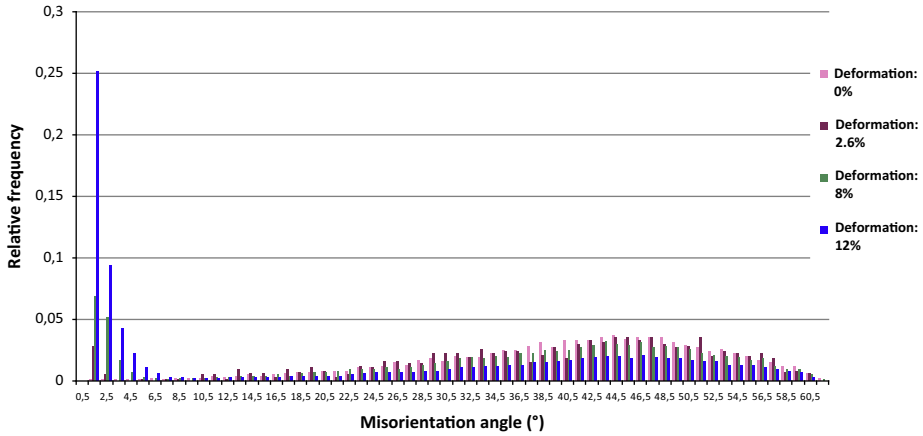

Fig. 4. Total correlated misorientation angle distributions measured on EBSD maps (from a minimum disorientation of 0.5°).

strain, the size of these voids increases (up to 40 µm) and their corresponding surface ratio also increases, especially for those with an ECD larger than 7 µm.

These voids are mainly localized at grain boundaries roughly aligned with the compression direction irrespective of shape, as already reported by Reynolds et al. [18]. In order to quantify this

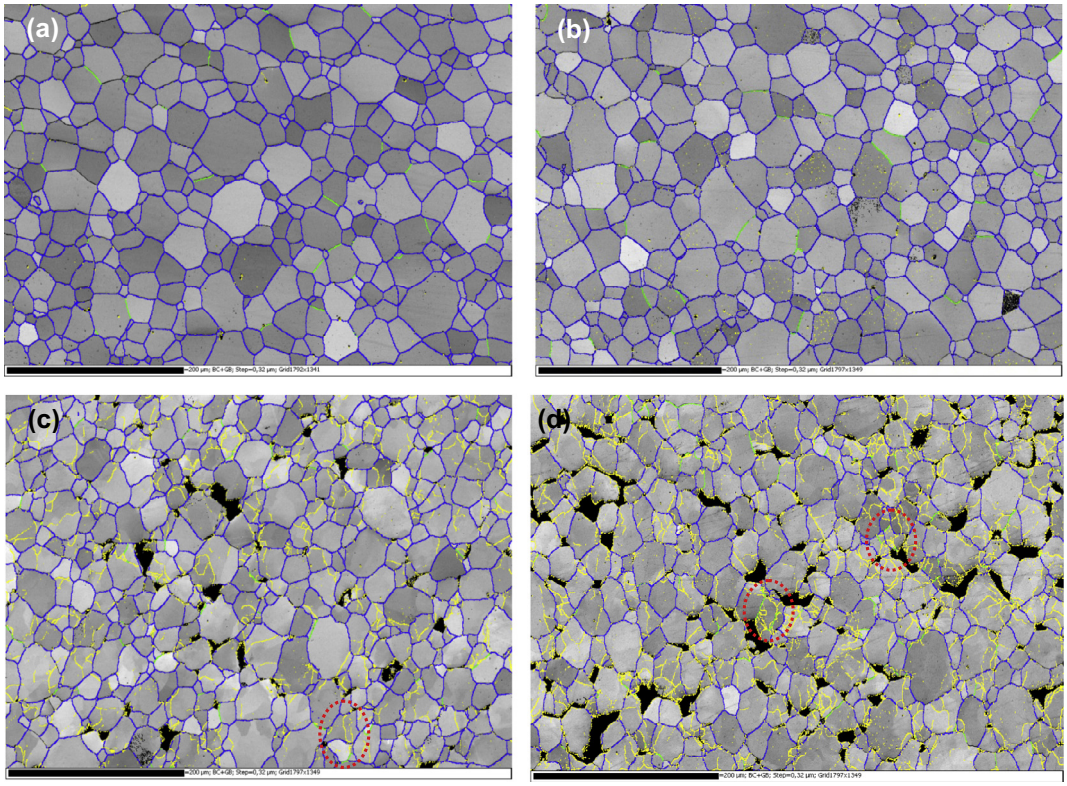

Fig. 5. EBSD maps (Kikuchi pattern quality + boundaries) obtained on (a) sample 1 (reference), (b) sample 2 (deformed at 2.6%), (c) sample 3 (deformed at 8%) and (d) sample 4 (deformed at 12%). Colour code chosen for boundaries misorientations: yellow $5° > \theta > 0.5°$, green $15° > \theta > 5°$, blue $\theta > 15°$.

tendency, the void orientation with respect to the compression axis was measured on samples 3 and 4 (voids in sample 2 were considered too small and too scattered to be characterized). Results showed that for both deformation levels (8% and 12%), about 40% of the voids had an inclination between 0° and 20°, about 33% between 20° and 45°, and about 27% above 45°. No clear correlation between the void size and their orientation was noticed.

Local EBSD maps revealed no specific disorientation range linked to intergranular void locations: boundaries with random disorientation distribution were evidenced, even in the sample deformed up to 12% (see Section 3.3).

3.2. Sub-grain boundaries evolution with deformation

With increasing deformation, dynamic recovery processes develop a pronounced substructure within the original grains and progressively creates new grains.

Fig. 4 corresponds to the misorientation angle distributions between neighbouring points measured on local EBSD maps performed on the four samples. It clearly shows a sharp increase with strain of the population of sub-boundaries for misorientation angles ranging between 0.5° (lowest misorientation accurately measurable) and 7°.

The development of the substructure is also demonstrated on coloured misorientation maps. In Fig. 5, Kikuchi pattern quality maps are superimposed with disorientation lines coloured according to the following code for misorientation angle θ: yellow for $5° > \theta > 0.5°$ (sub-grain boundaries), green $15° > \theta > 5°$ (low angle grain-boundaries), blue $\theta > 15°$ (high angle grain-boundaries). In the reference sample (Fig. 5a), most of the grain-boundaries are high angle ones and no sub-grains are observed. It is almost the same for sample 2 (Fig. 5b), the yellow dots present on this map corresponding to measurement noise (0.5° being close to the angular limit of accuracy for EBSD measurements). Conversely, for samples 3 and 4 (Fig. 5c and d), well defined yellow lines are observed, even if they are not always continuous and/or disturbed, for example close to intergranular voids (which appear in black, on these maps). These lines, which are characteristic of sub-grain boundaries, become more numerous when the deformation level increases. They delimitate sub-grains with a size ranging from a few to ten micrometres. In certain cases (cf. red dotted encircled areas, in Fig. 5c and d), they reach a misorientation value greater than 5°, defining new low angle grain-boundaries (green lines).

The increase of sub-structured grain surfaces fraction was quantified from the EBSD data by building "sub-structured fraction maps", as defined in the EBSD post processing software [16]. These maps define three types of grains: (i) grains with low internal disorientations, which are almost not affected by the deformation process (in blue), (ii) grains with internal disorientations organized in sub-grains (sub-structured) (in yellow), (iii) grains with "anarchical" internal disorientations (deformed) (in red). Fig. 6 shows the results on the global EBSD map: the sub-structured surface went from almost zero in samples 1 and 2, to about 40% in sample 3 and about 50% in sample 4 (the critical disorientation angles chosen as thresholds for defining grains and sub-grains were respectively 5° and 1°). It is also worth noting that deformed areas were small and scattered, generally located at triple points and/or close to intergranular voids brought about by creep.

The conventional EBSD analysis, with an angular resolution of the order of 0.5°, cannot quantify lower cellular substructure also produced by dynamic recovery. This limitation is illustrated in Figs. 7a and b. The SEM micrograph, taken of sample 3 (deformed at 8%), in BSE mode (Fig. 7a), reveals numerous sub-grains characterized by more or less sharp changes of grey levels within certain grains (such as the two large ones located in the centre of the micrograph). In Fig. 7b, which corresponds to an EBSD map of the same area of the sample, in optimized conditions for detecting low disorientations (for example no camera binning, maximal

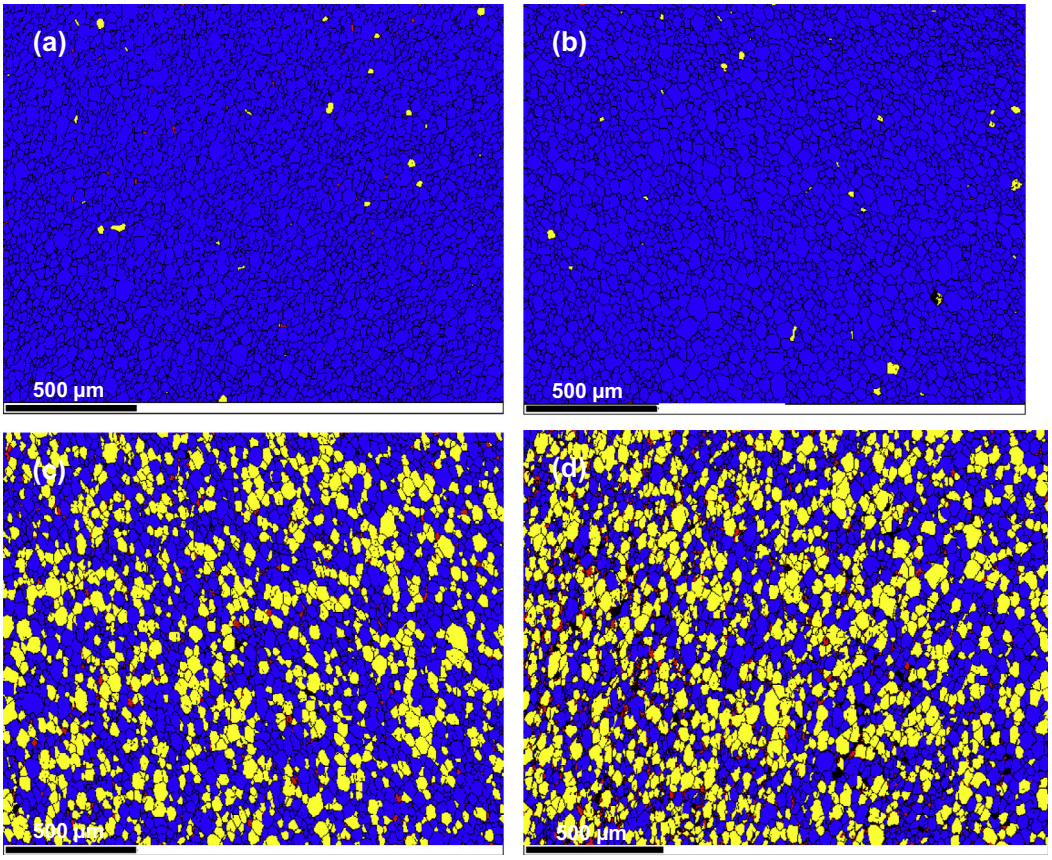

Fig. 6. EBSD maps in sub-structured fraction (in yellow) for (a) sample 1 (reference), (b) sample 2 (deformed at 2.6%), (c) sample 3 (deformed at 8%) and (d) sample 4 (deformed at 12%) (blue and red areas respectively correspond to not deformed and deformed grains).

Hough resolution, etc), only a fraction of these sub-grains are revealed. In fact, if those corresponding to disorientations greater than 0.5° (yellow lines) are relatively well defined, those corresponding to lower disorientations (cf. red lines, for disorientations between 0.3° and 0.5°) are only partly delimited or even not detected at all (cf. two encircled areas by white dotted lines, in Figs. 7a and b, for example). Deeper microstructure analysis, by performing high resolution observations in electron channeling contrast imaging (ECCI) conditions [15], confirms that lower angle boundaries are clearly present in the 8% and 12% deformed samples. Indeed, dislocation arrangements along low angle boundaries can be observed, as illustrated by Fig. 7c. They define cells with sizes ranging from one to several micrometres. In these types of images, where dislocations are revealed, a pinning effect by intragranular pores of mobile dislocations seems to be involved and could therefore affect the development of the substructure.

Finally, with increasing deformation, this substructure progressively creates new grains with boundaries disorientated by more than 5°, as already noticed in Fig. 5. This evolution is quantified in Fig. 8 which shows the grain size distribution in the four studied samples, as determined from EBSD data (with a critical disorientation angle for grain boundaries fixed at 5°). A significantly greater fraction of small grains (size: below 15 µm) is present in sample 4 (deformed up to 12%). This evolution is linked to the development of substructures within the original grains, which progressively leads to the creation of new grains with boundaries disoriented by more than 5°.

Despite this feature, which concerns only a relatively small proportion of the grains in sample 4, no significant modification of the mean grain size occurred after the creep test. This size ranges between 25 µm and 27 µm, depending on the sample and can be considered as unchanged, taking into account the accuracy of the EBSD measurements (~10%) and the intrinsic microstructural dispersion encountered in UO_2 fuel pellets (generally of the order of 20%, knowing that only one area per sample was analysed in this study).

3.3. Grain shape and orientation changes

It is generally assumed in the literature that creep deformation of UO_2 pellets during compression tests does not induce a significant change in the grain shape, which remains equiax (at least in testing conditions and deformation levels close to those considered in this work) [19,6]. This characteristic is generally interpreted as a consequence of a grain boundary sliding (GBS) mechanism without grain deformation.

In order to check this point, the shape of the grains detected on EBSD maps was studied by means of the aspect ratio (ratio of major over minor axis) of fitted ellipses. In Fig. 9, grains with an aspect ratio greater than 2 are delineated by black lines and coloured according to the colour scale indicated in Fig. 9e. Most of them are green, indicating that their aspect ratio generally ranges between 2 and 3. These grains are scarce and scattered in the reference sample (Fig. 9a), whereas they become more numerous and take up a preferential morphological orientation, when the deformation increases: this orientation is mostly vertical on the maps, i.e. perpendicular to the compression direction. The surface fraction associated with this population of elongated grains grows from about 5% in samples 1 and 2, to 8% in sample 3 and 14% in sample 4. It is worth noting that elongated grains are not always homogeneously distributed and oriented in each area (cf. Fig. 9d, in particular). This is due to the fact that the major deformation area is not always "perfectly" centred in the pellet, probably

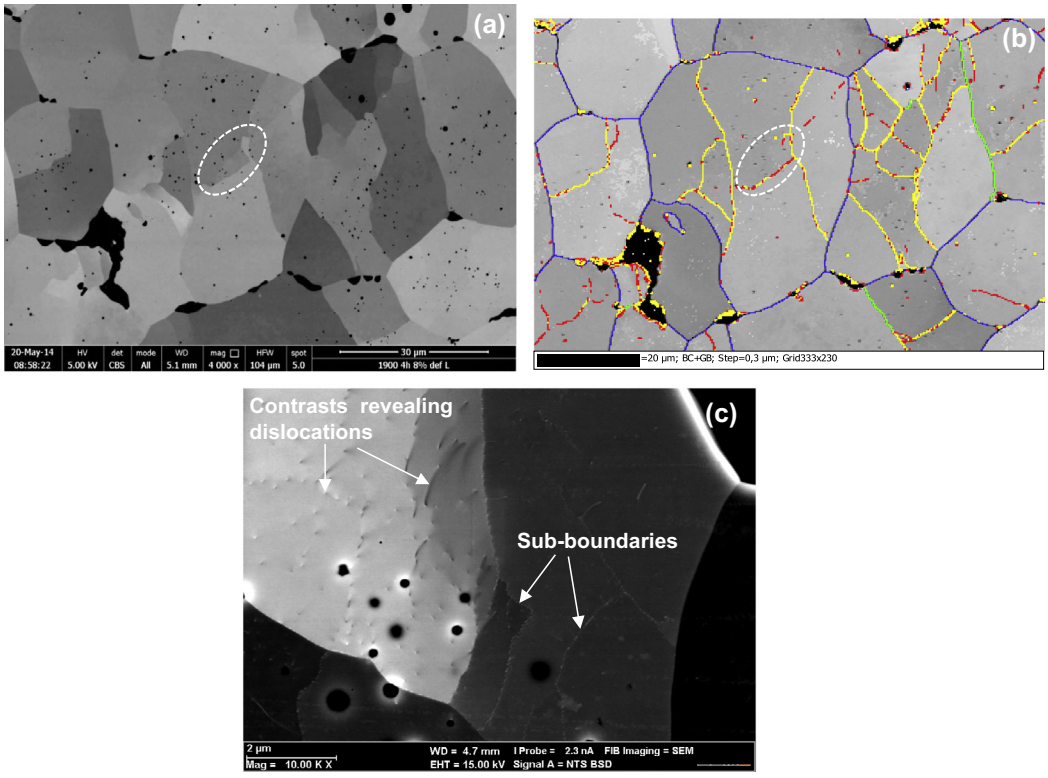

Fig. 7. (a) SEM micrograph in BSE mode, (b) corresponding EBSD map in Kikuchi pattern quality + boundaries (colour code chosen for boundaries misorientations: red $0.5° > \theta > 0.3°$, yellow $5° > \theta > 0.5°$, green $15° > \theta > 5°$, blue $\theta > 15$) and (c) SEM micrograph taken in electron channeling contrast conditions (sample 3, deformed at 8%).

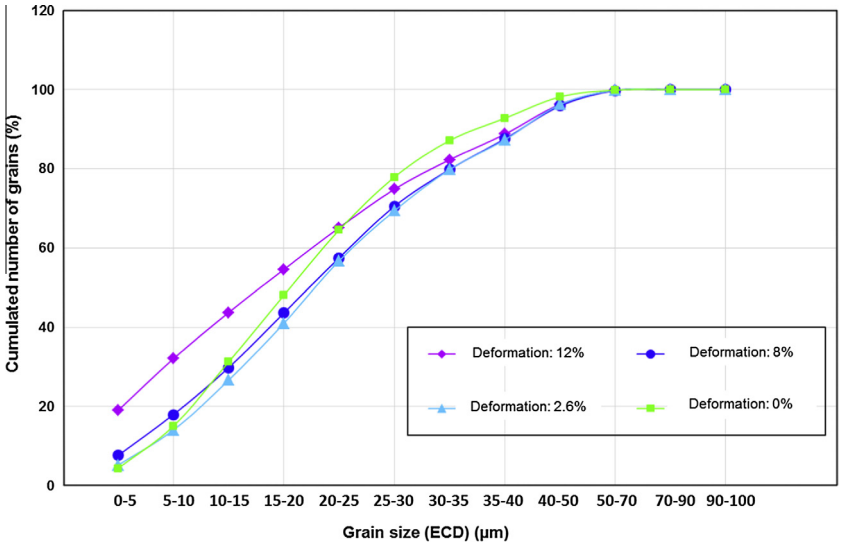

Fig. 8. Grain size evolution with deformation.

because of physical heterogeneities and/or slightly heterogeneous conditions of mechanical loading.

Even if a relatively low fraction of grains appears elongated after the test, their presence indicates that sliding mechanisms, with plastic deformation, took place during the creep process.

A slight texture development was also detected with the deformation. Figs. 10a and b presents the pole figures obtained from all grains (about 6000 per sample), in contouring mode (to evidence an eventual pole clustering), for samples 1 and 4 (reference and deformed at 12%). The projection plane is perpendicular to the compression direction. The orientation distribution is almost random for the reference sample, whereas a slight clustering of ⟨1 1 0⟩ poles are observed close to the compression direction after deformation, as clearly evidenced by the corresponding inverse pole figure (Fig. 10c). This clustering reflects an increase of the number of grains that align a ⟨1 1 0⟩ direction close to the compression direction. This corresponds typically to the texture fiber that develops by hot compression of fcc material [20].

The slight changes in grain morphology and in orientation distribution indicate that crystallographic slip of dislocations is an

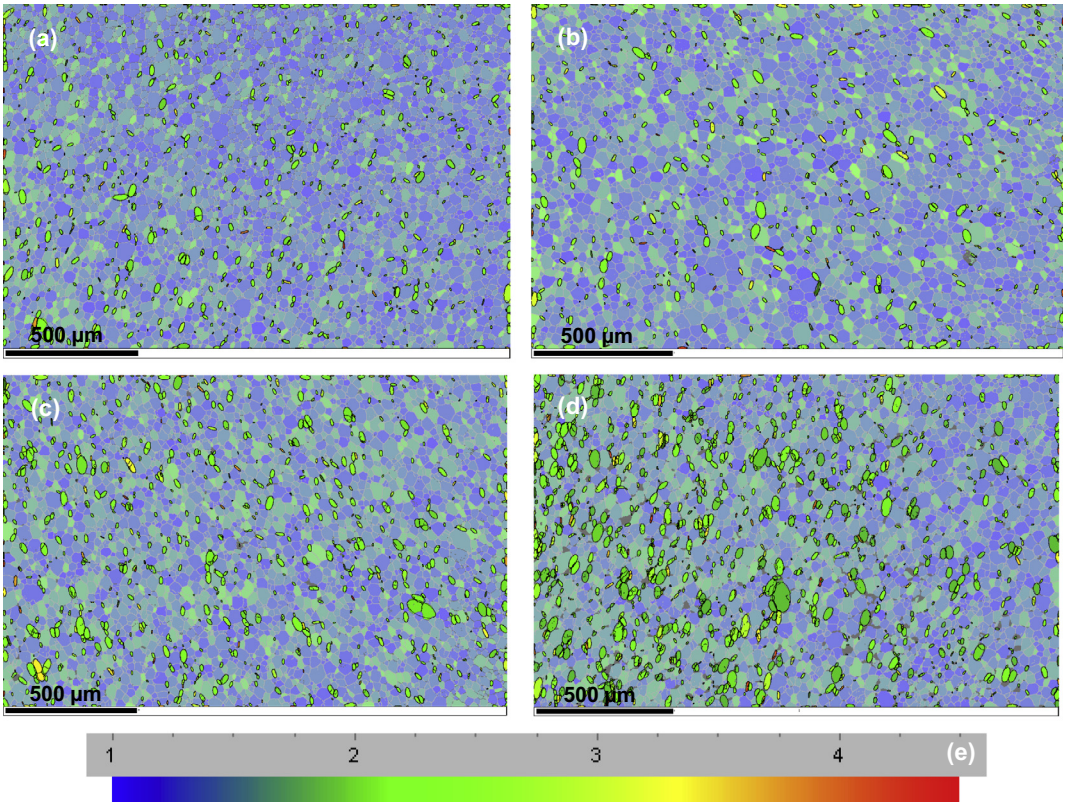

Fig. 9. Aspect ratio maps for (a) sample 1 (reference), (b) sample 2 (deformed at 2.6%), (c) sample 3 (deformed at 8%) and (d) sample 4 (deformed at 12%). Grains with an aspect ratio greater than 2 are delineated in black by fitted ellipses and coloured according to the colour scale indicated in (e).

additional deformation mechanism to grain boundary sliding for the accommodation of the macroscopic deformation.

4. Discussion

Four UO_2 samples deformed from 0 (reference state) to 12% as a result of compression creep tests performed in the "high stress" creep regime were studied. Thanks to SEM micrographs coupled with image analyses and EBSD maps, features concerning intergranular voids, grains and sub-grains, were obtained. These features are summarised and discussed hereafter in terms of creep mechanisms.

There are few small intergranular voids induced by creep at a low deformation level (2.6%). Most of these voids are located between two (adjacent) grain faces, a few appearing at triple points. Their rounded shape tends to indicate that their formation is associated with diffusion mechanisms. In fact, at this stage of the deformation process, intergranular fabrication pores can act as traps for vacancies, leading to a coarsening and finally a percolation of these pores, as already observed in UO_2 at low stresses [6] and also in other sintered ceramics [21] [22]. When the deformation increases, diffusion mechanisms and grain boundary sliding compete, leading to the coexistence of two types of voids: lenticular and crack-like, both being predominantly located on boundaries relatively parallel to the compressive stress axis, in accordance to Reynolds et al.'s observations [18]. Finally, at high deformation levels, sliding mechanisms become predominant and well developed crack-like voids, with a wider range of orientations, are encountered.

The mean grain size of the samples, measured by EBSD, did not significantly change during creep tests. Pole figures obtained on a large population of grains (about 6000 grains per sample) showed that slight modifications of the grain orientations appeared with deformation. These modifications could be due to rotation phenomena of certain grains, accommodating deformation processes. They lead to an increase in the number of grains aligned along a $\langle 1\,1\,0 \rangle$ direction close to the compression direction, as typically observed after hot compression of fcc materials [20]. To the best of our knowledge, such fibre texture development has never been demonstrated on creep tested UO_2 samples.

EBSD maps also allowed us to determine that a small fraction of the grains (about 14%, in the sample deformed up to 12%) became elongated perpendicularly to the compression direction. This result is quite original, since it is generally assumed that creep deformation of UO_2 in conditions close to those chosen in this study does not lead to a change in form of the grains [6] [19]. It is consistent with creep processes considered in different ceramics [23] and indicates that plastic deformation and sliding processes, within the grains, are also involved in the creep process.

EBSD is particularly well adapted to the characterization of the sub-structure development in UO_2. It shows that, in the samples deformed up to 8% and 12%, numerous sub-grains, with a size ranging from one to several micrometres, are present. These sub-grains are characterized by low misorientations, which are not all measurable by conventional EBSD (for those lower than 0.5°). HR-EBSD method, using a cross-correlation software, could allow a better detection of sub-grains boundaries. ECCI imaging is also a powerful and promising complementary tool for studying them. It could help to understand interactions between fabrication pores (especially intragranular ones) and dislocations and their implications in the sub-structuration process.

Global sub-structured area maps allowed us to conclude that, at a deformation level of 12%, about 50% of the surface (in the central part of the pellet) contained sub-structured grains. Local maps showed this sub-structure development more clearly. It progressively leads to the occurrence of new low angle boundaries, defining new small grains. These results are on the whole consistent

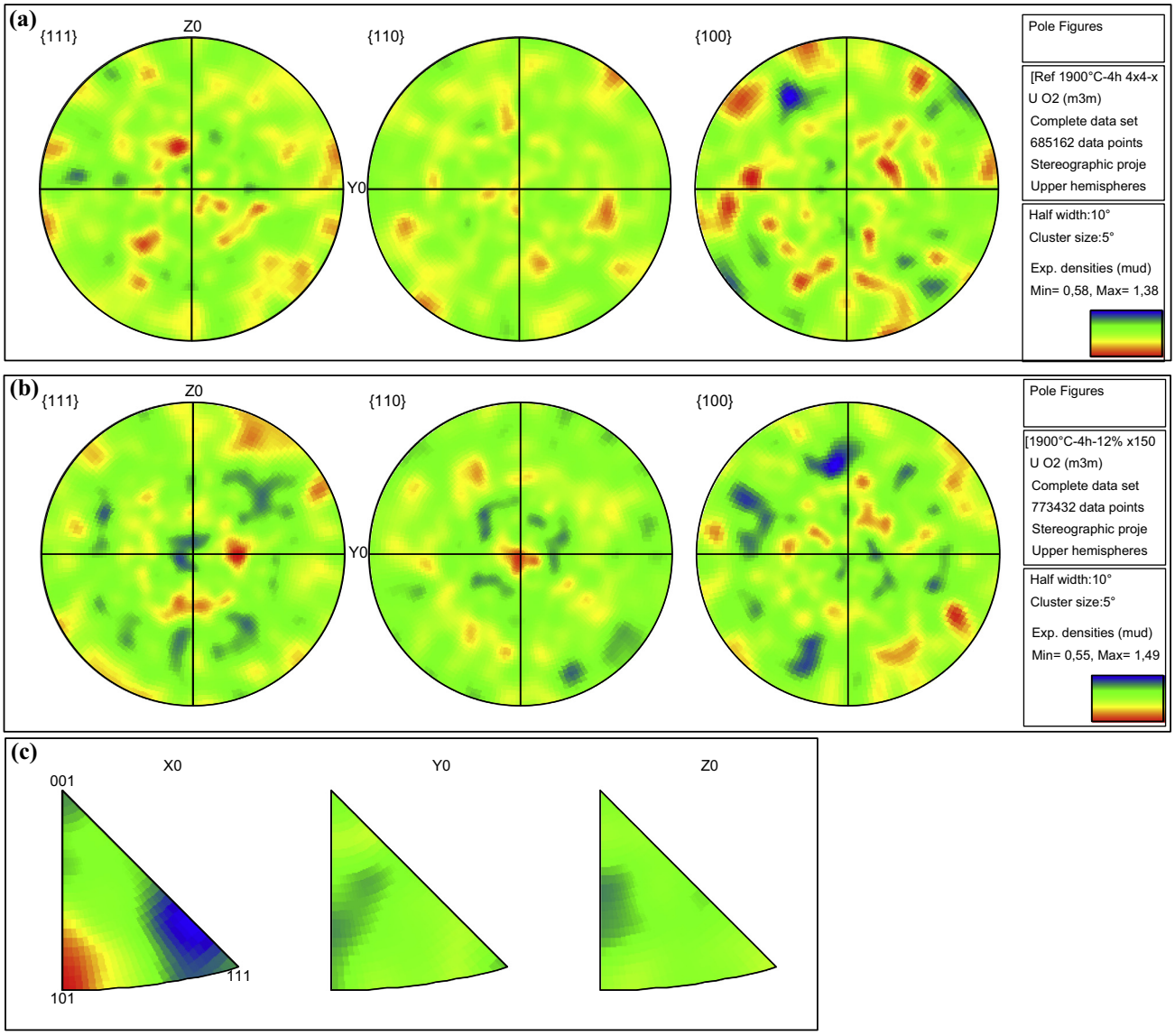

Fig. 10. Pole figures (in contouring mode) of (a) sample 1 (reference), (b) sample 4 (deformed at 12%) and (c) inverse pole figure (in contouring mode) of sample 4.

with those previously obtained by several authors, thanks to TEM examinations performed on single-crystals [24] [25] or polycrystals [6], on cell boundaries, but they concern much larger areas (of the order of 1 mm^2) and allows (at least partly) a quantification of the sub-structuration process. This division process into cells, occurring within the grains, could perhaps explain why a relatively small increase of the elongated grain surface fraction (from 8% to 14%, respectively for 8% and 12% of deformation) was observed when increasing the deformation level, some of these grains being divided into new ones.

For our sample characteristics (grain size: about 25 μm) and testing conditions (1500 °C, 50 MPa), according to our results and to the literature, it seems reasonable to assume that:

- At low deformation levels (about 2.5%), deformation mainly implies a diffusional material transport, in which fabrication pores are involved.
- At higher deformation levels (8–12%), slip systems are activated within the grains, and numerous dislocations appear. These dislocations probably facilitate diffusion creep mechanisms, which presumably remain active. A dynamic recovery process takes place and results in the organization of a large part of the dislocations into sub-boundaries, dividing grains in micrometric sub-grains, with low misorientations. At the same time, intergranular decohesion process by grain boundary sliding becomes more and more active.

So, the deformation process of UO_2 seems to globally imply three probably concomitant mechanisms, as described in a general case by Crossman [26]: (i) diffusional creep, (ii) dislocational creep within the grains, (iii) grain boundaries sliding. This description is also globally consistent with that given by [6]. The relative contributions of these different mechanisms to the macroscopic deformation of the pellet very likely varies with the loading conditions (temperature, compressive stress, strain rate...), the local mechanical state, and microstructural characteristics, such as the size and distribution of fabrication pores.

Finally, it is worth noting that the EBSD method appeared really well adapted to the study of UO_2 deformation processes, especially the characterization of sub-structuration phenomena observed within the grains.

5. Conclusion

This work was aimed at studying the damage process in UO_2 during creep tests, in the "high stress" creep stage. For this purpose, UO_2 pellets with relatively large grains ($\sim$25 μm) were tested at 1500 °C under a compressive stress of 50 MPa, at different deformation levels up to 12%. Image analyses of SEM images were performed to characterize void development in the microstructure and Electron Back Scattered Diffraction (EBSD) was used to follow the evolution, with deformation, of grains (size, shape, orientation) and sub-grains.

EBSD proved to be a very interesting tool for studying UO_2 deformed samples. It enabled us to demonstrate a slight evolution of the orientation of the grains after deformation. It also revealed an evolution of the shape of certain grains, which became elongated perpendicularly to the compression direction. It pointed to the occurrence of a slight fibre texture and the development of sub-structures within the grains and allowed to follow it.

Further work is planned to acquire complementary results on a larger range of loading conditions, on samples with different microstructural characteristics.

Acknowledgments

E. Bertrand, J.P. Alessandri, M. Salvo and J. Sanchez (from CEA/Cadarache) are warmly thanked for the elaboration, the mechanical tests and the metallographic preparation of the samples. The authors are also grateful to H. Rouquette and N. Tarisien (from CEA/Cadarache) for performing the SEM and EBSD characterizations. They also thank Ph. Garcia (from CEA/Cadarache) for his careful reading of this paper.

References

[1] D.D. Baron, L. Hallstadius, Compr. Nucl. Mater. 2 (19) (2012) 481–514.
[2] B. Michel, J. Sercombe, C. Nonon, O. Fandeur, Compr. Nucl. Mater. 3 (22) (2012) 677–712.
[3] Y. Guérin, J. Nucl. Mater. 56 (1975) 61–75.
[4] M.S. Seltzer, J.S. Perrin, A.H. Clauer, B.A. Wilcox, React. Technol. 14 (1971) 99–135.
[5] D.B. Knorr, R.M. Cannon, R.L. Coble, Acta Metall. 37 (1989) 2103–2123.
[6] F. Dherbey, F. Louchet, A. Mocellin, S. Leclercq, Acta Mater. 50 (2002) 1495–1505.
[7] J.C. Gao, L.F. Liang, Y. Wang, S.F. Fang, Trans. Nonferr. Met. Soc. China 20 (2010) 238–242.
[8] F.H. Humphreys, J. Mater. Sci. 36 (2001) 3833–3854.
[9] D. Stojakovic, Proc. Appl. Ceram. 6 (2012) 1–13.
[10] P.V. Nerikar, K. Rudman, T.G. Desai, D. Byler, C. Unal, K.J. McClellan, S.R. Phillpot, S.B. Sinnott, P. Peralta, B.P. Uberuaga, C.R. Stanek, J. Am. Ceram. Soc. 94 (2011) 1893–1900.
[11] E. Pizzi, P. Garcia, G. Carlot, H. Palancher, S. Maillard, B. Pasquet, I. Roure, C. Pozo, C. Maurice, Forum 323–325 (2012) 197–202.
[12] K. Rudman, P. Dickerson, D. Byler, R. McDonald, H. Lim, P. Peralta, C. Stanek, K. McClellan, Nucl. Technol. 182 (2013) 145–154.
[13] M. Teague, B. Gorman, B. Miller, J. King, J. Nucl. Mater. 444 (2014) 475–480.
[14] A. Ndiaye, PhD Thesis, University of Grenoble, France, 2012.
[15] H. Mansour, J. Guyon, M.A. Crimp, N. Gey, B. Beausir, N. Maloufi, Scripta Mater. 84–85 (2014) 11–14.
[16] Oxford Instruments, Channel 5, February 2010 (http://www.oxinst.com).
[17] NF ISO 13067, AFNOR standard (France), January 2012.
[18] G.L. Reynolds, B. Burton, M.V. Speight, Acta Metall. 23 (1975) 573–577.
[19] T.E. Chung, T.J. Davies, Acta Metall. 27 (1979) 627–635.
[20] A. Kumar, P.R. Dawson, J. Mech. Phys. Solids 57 (2009) 422–445.
[21] J.R. Porter, W. Blumenthal, A.G. Evans, Acta Metall. 29 (1981) 1899–1906.
[22] C.R. Blanchard, K.S. Chan, J. Am. Ceram. Soc. 76 (1993) 1651–1660.
[23] A.H. Chokshi, J. Eur. Ceram. Soc. 22 (2002) 2469–2478.
[24] A. Alamo, J.M. Lefevre, J. Soullard, J. Nucl. Mater. 75 (1978) 145–153.
[25] R.J. Keller, T.E. Mitchell, A.H. Heuer, Acta Metall. 36 (1988) 1073–1083.
[26] F.W. Crossman, M.F. Ashby, Acta Metall. 23 (1975) 425–440.